Nanoscale

Cite this: *Nanoscale*, 2011, **3**, 4685

www.rsc.org/nanoscale

PAPER

Nanoporous artificial proboscis for probing minute amount of liquids

Chen-Chih Tsai,[a] Petr Mikes,[b] Taras Andrukh,[a] Edgar White,[a] Daria Monaenkova,[a] Oleksandr Burtovyy,[a] Ruslan Burtovyy,[a] Binyamin Rubin,[a] David Lukas,[b] Igor Luzinov,[a] Jeffery R. Owens[c] and Konstantin G. Kornev*[a]

Received 8th July 2011, Accepted 25th August 2011
DOI: 10.1039/c1nr10773a

We describe a method of fabrication of nanoporous flexible probes which work as artificial proboscises. The challenge of making probes with fast absorption rates and good retention capacity was addressed theoretically and experimentally. This work shows that the probe should possess two levels of pore hierarchy: nanopores are needed to enhance the capillary action and micrometer pores are required to speed up fluid transport. The model of controlled fluid absorption was verified in experiments. We also demonstrated that the artificial proboscises can be remotely controlled by electric or magnetic fields. Using an artificial proboscis, one can approach a drop of hazardous liquid, absorb it and safely deliver it to an analytical device. With these materials, the paradigm of a stationary microfluidic platform can be shifted to the flexible structures that would allow one to pack multiple microfluidic sensors into a single fiber.

Introduction

Many butterflies, moths, and other insects easily probe and identify potable liquids with their proboscises. The ability to manipulate the proboscis, which can be coiled and uncoiled like a party noisemaker, is closely linked to its remarkable fluid transport capabilities. In addition, the proboscis can be flawlessly positioned in a targeted liquid drop. Insect proboscises feature integrated sensors and filters that distinguish foods and chemicals. Integrating all these features—ability to deploy, sense and sample, and identify low-volume fluids—into a single micro–nanofluidic device is attractive and promising for many engineering applications. Therefore, it becomes a challenging and rewarding task to fabricate an artificial, biomimetic proboscis that possesses many properties of its natural cousin.

As recently shown by our group, the butterfly proboscis has a two-level pore hierarchy.[1] The proboscis is nanoporous in its lateral dimension, which comprise the first level of pore hierarchy. These nanopores are created by overlapping legulae. The legulae are formed like a fence on two tubular musculature structures—galeas, Figure 1. Galea tubes have lateral semi-cylindrical indentations, so that when galeas are locked by legulae, these two indentations form the food canal. The food canal, whose diameter ranges from a few to tens of micrometers, forms the second level of pore hierarchy. Thus, the proboscis can be considered as a drinking straw with a nanosponge.[1]

In this paper we apply this natural structural organization to design a probe that simultaneously has a strong driving suction pressure and sufficiently fast wicking rate. We show that the probe material requires at least a two-level pore hierarchy consisting of nanometer pores that provide strong capillary action, and micrometer pores that provide rapid wicking.

We focus our efforts on materials and design strategies for making artificial proboscises that feature an unprecedented

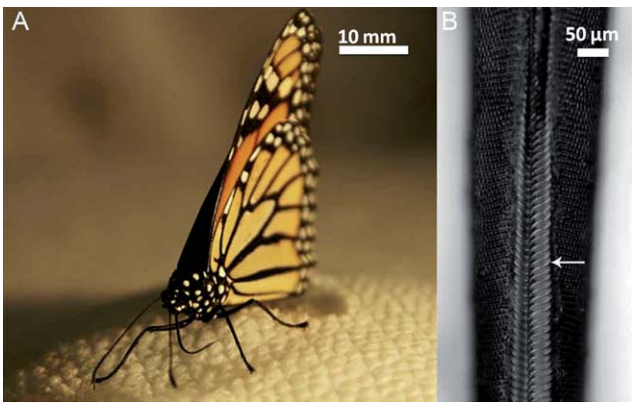

Fig. 1 (A) Butterfly drawing sugar solution from paper towel. The dorsal side of the proboscis is pushed toward the porous surface, (B) Magnification of the proboscis. One can see the central groove with the legulae (shown by the arrow) looking like a fence at the dorsal side of the proboscis. The liquid wicks into the food canal through the nanopores formed by two nearest legulae.

[a]*School of Materials Science & Engineering, Clemson University, 161 Sirrine Hall, Clemson, SC, 29634-0971, USA. E-mail: kkornev@clemson.edu; Fax: +1-864-656-5973*
[b]*Faculty of Textile Engineering, Technical University of Liberec, Halkova 6, 461 17 Liberec, Czech Republic*
[c]*Air Force Research Laboratory, Airbase Tech. Div., Airbase Sci. Branch, Tyndall AFB, Panama City, FL, 32403, USA*

flexibility, deployability, and absorptive capacity, using electrospun nanofibers as building blocks for these micro- and nanofluidic devices. Recently, electrospun nanofibers have gained considerable attention as building blocks for various constructs and nanodevices.[2–6] Nanofibers can be made porous and hollow, and can be bundled and twisted into yarns. These materials constitute a broad class of flexible, lightweight structures that can be utilized in many applications dealing with liquid handling and manipulation.[7–12]

Different ideas and demonstrations of yarn formation from electrospun nanofibers have been recently reported in the literature,[13–21] but neither approach has been proven to provide materials with reproducible diameters, and transport and mechanical properties. Precision control of these properties, however, is critical for the probe performance. We therefore focused on the development of an industrially scalable method of yarn formation that would provide reproducible wetting, wicking, and mechanical characteristics for these yarns. As an illustration of robustness of the proposed method, we made an artificial proboscis from polyvinylidene fluoride (PVDF) fibers. PVDF is one of the most difficult polymers to electrospin because it must be heated during the electrospinning process. On the other hand, PVDF is legendary for its chemical inertness and thermal stability due to the presence of -CF_2- groups.[53] Another advantageous PVDF property is that the $C_2H_2F_2$ molecular units of the polymer chains possess large dipole moments. These dipoles point from the electronegative fluorine to the electropositive hydrogen.[53] Under certain solidification conditions, the dipoles form ordered structures that make the material ferroelectric.[53] Hence, the produced probes can be manipulated with electric fields to grab and absorb distant droplets of hazardous liquids. The PVDF fibers can be made porous by adding a removable polymer to the dope prior to electrospinning. As an example, we used poly(ethylene oxide) (PEO) as the removable polymer, and experimentally confirmed that the probes made of these nanoporous fibers do exhibit an increased rate of liquid absorption. We demonstrated the performance of the artificial proboscis by absorbing droplets of tributyl phosphate (TBP), a popular simulant of hazardous liquids and a solvent for many hazardous chemicals.[22–28]

We believe that artificial proboscises made of nanofibers with the proposed pore structure will find many applications as active elements in nanofluidic devices, chemical and biomedical sensors, forensic probes, and in many other fields where probing minute amounts of liquids is a crucial step of material processing and analysis.

Results and discussion

Fabrication of artificial proboscis

Electrospinning appears to be the simplest and most inexpensive technique for the fabrication of nanofibers, Figure 2.[2–5,21,29] In electrospinning, the polymer solution to be spun is charged to a high voltage that is typically measured in kilovolts. When the charge is sufficient to overcome the surface tension of the solution, the surface of the polymer solution undergoes a sudden transformation from flat to a cusped, followed by emanation of a jet. On its way to the oppositely charged collector, the jet bends and twists causing the polymer to stretch. Simultaneously, the solvent evaporates, leaving behind a nanoscopic polymeric filament on the collector. These filaments can then be made into yarns.[13–15] However, the reproducibility of the transport and mechanical properties of these yarns has not been demonstrated.[2,21,30,31]

To form the probe we propose an industrially scalable method consisting of two steps: in the first step, one needs to prepare an array of oriented fibers, as shown in Figure 3A, which can be gathered on the second step by using a special device shown in Figure 3B. This device has a twofold purpose: it collects the nanofibers and then twists them into a yarn. The proposed method takes advantage of the most popular methods of formation of ordered fiber arrays suggested in Ref.32. Recent developments of this idea were reviewed in Ref.21. As shown in Ref.32 fiber ordering can be significantly increased if a target electrode is made of unipolar parallel plates. Near the plates, the electric field calculated using COMSOL® modeling software is almost two-dimensional, as demonstrated in Figure 2B (the model parameters are described in the section on Probe manufacturing). Since both plates are kept at the same voltage, the electric field lines branch out from a singular line, which divides the interplate gap in halves. Near the two charged plates, the electric field vector $\boldsymbol{E}$ has opposite directions. Therefore, if two identical charges q are situated in different halves of the interplate gap, they will be pushed by the force $\boldsymbol{F} = q\boldsymbol{E}$ toward different plates. For the jet, this specific electrode geometry works as a natural stretching device. As a charged jet approaches the electrodes and is about to land in between, the electric force pulls the jet in different directions. Because the nanofibers are charged, they repel each other. As a result, the nanofibers align perpendicular to the plates. To collect more nanofibers, it is convenient to use a mandrel with four or more metal arms, such as those implemented in our device shown in Figure 2A. Each pair of aluminum bars collects a band of oriented nanofibers, Figure 3A.

After collection of oriented nanofibers, one has to harvest the nanofibers from the mandrel. We designed a special device for fiber collection consisting of two circular wire brushes mounted co-axially and attached to two miniature DC motors. The two arms of the collector support the rolled brushes, Figure 3B. The nanofibers are gathered as a fibrous cylindrical shell attached from its ends to the brushes. The same device is used to form yarns by spinning the brushes in opposite directions: the brushes twist the nanofibrous shell to a predetermined density, thus forming a yarn. The yarn twisting device allows one to control the yarn diameter and density by changing the total number of revolutions of the supporting brushes (see Methods for details). After twisting, the yarn was cut into pieces to form the fiber-based probes. Using this method, we formed yarns from PVDF/PEO blends.

Nanoporous artificial proboscises from PVDF/PEO blends: Properties

Proboscis characterization: Scanning Electron and Optical Microscopy. The morphological structure of the PVDF/PEO nanofiber surfaces and yarns was examined with a Hitachi Field Emission scanning electron microscope (FESEM-Hitachi 4800).

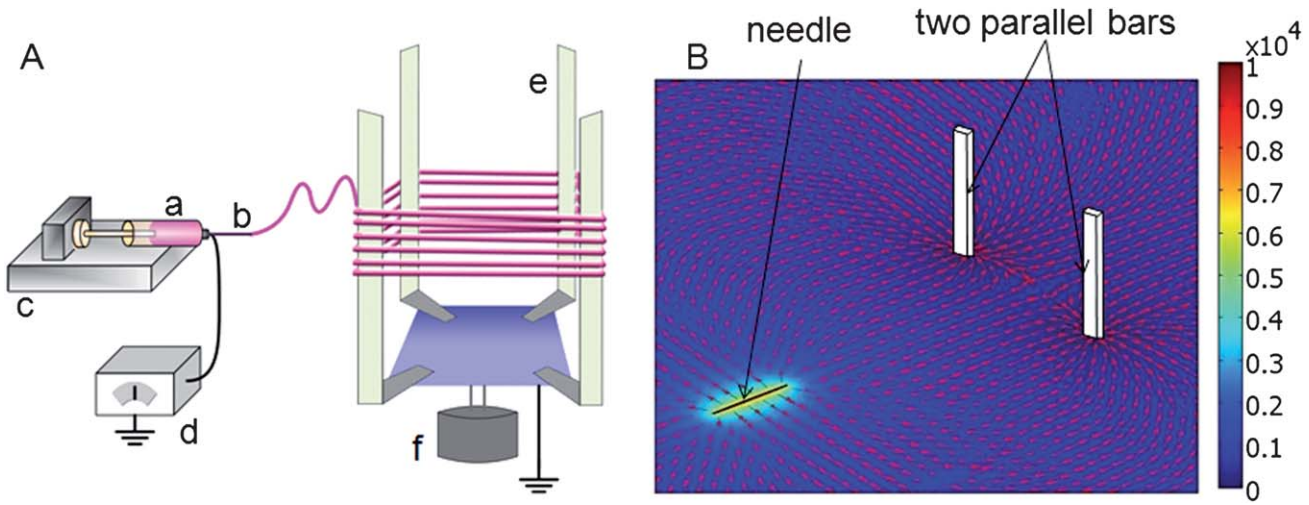

Fig. 2 (A) Schematic diagram of the electrospinning apparatus for collecting nanofibers. (a) syringe with polymer solution, (b) metal needle, (c) syringe pump, (d) high-voltage power supply, (e) rotating collector, (f) motor. (B) The perspective view of electric field in the region between the needle and two-arm collector. The red arrows denote the direction of the electrostatic field, and different colors in the plane correspond to different potentials specified in the vertical bar. The needle is charged to 10 kV and the bars are grounded.

Figure 4B shows the typical morphology of PVDF/PEO nanoporous fibers after dissolution of PEO in water. The fiber diameters range between 0.8 and 1.8 μm, giving an average diameter of ~1.2 μm. During our experiments, we discovered that nanoporous fibers can be produced without the PEO removal step by spinning the fibers at 60 ± 5% ambient relative humidity (RH).

We employed optical microscopy (Olympus BX-51) to examine the reproducibility of the artificial proboscises. Several sets of PVDF/PEO yarns were electrospun under identical conditions. The time of electrospinning and twist rate were varied. Measurements of yarn diameter were taken at 10 points along each yarn. Figure 3F shows the diameters of eight different yarns averaged over 10 points each. As shown, the yarns have reproducible average diameters. The thicker the fiber band to start with, the easier it is to produce yarns with reproducible diameters. The thinnest reproducible yarns in this work were 20 μm in diameter.

Elastic properties of fibers and yarns. The advantage of using PVDF-based probes is that the probes can be manipulated by electric fields. These manipulations can be used to interrogate distant droplets or other objects. Therefore, the probe needs to be made from very flexible fibers. For fluid probing applications, we used porous fibers. Their elastic modulus is difficult to predict. Hence, to experimentally evaluate the elasticity of a single PVDF/PEO fiber we used an atomic force microscope (Dimension 3100 AFM, Veeco Inc). We used the method described in Ref.33, but adjusted our set-up to measure the equilibrium forces and elongations rather than the dynamic non-equilibrium forces

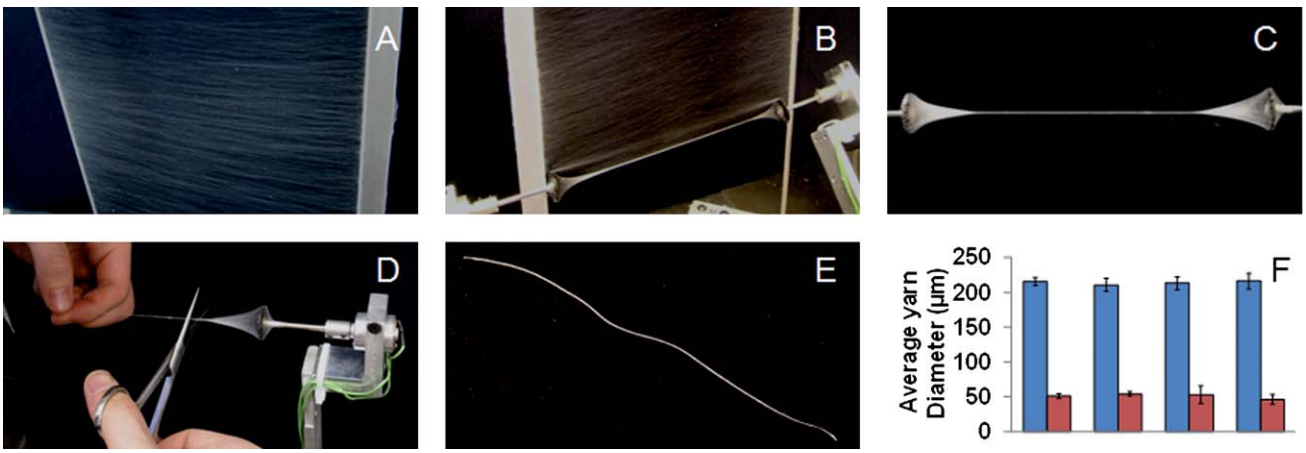

Fig. 3 Steps of yarn formation: (A) Ordered nanofibers forming a band on the two-arm collector. (B) Gathering nanofibers with the brushes moving along the electrodes–rails. (C) Yarn formed after 120 twists. (D) Taking off the yarn by scissors. (E) The produced yarn. (F) Chart showing the reproducibility of the yarn diameter. The red column represents the average yarn diameter after a 15 minute collection. One-hundred and twenty twists were applied. The blue column represents the average yarn diameter of an hour long collection. One hundred twists were applied. The error bars show the standard deviations.

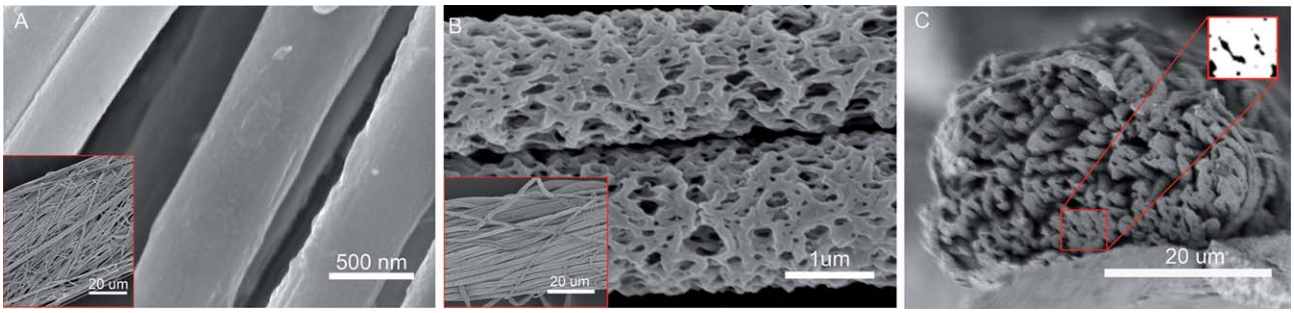

Fig. 4 SEM images of the electrospun PVDF/PEO fibers. (A) Solid non-porous fibers, (B) Porous fibers, (C) The cross-section of PVDF/PEO yarns. The black areas in the insert show the pores in an undisturbed spot after the yarn cutting. This area suggests that the porosity is close to 10%.

and deformations reported in Ref.33. For this experiment, a monolayer of the fiber web was electrospun onto a silicon wafer (SEH America Inc.). A drop of epoxy glue was placed on the wafer surface. A single fiber was located with the AFM and cut out by the AFM tip to the size of several hundred micrometers. Another end was attached to the AFM cantilever by epoxy glue as discussed in Ref.34. Following these preparations, the AFM cantilever was moved up in 1 μm increments, while the voltage signal corresponding to the vertical deflection of the cantilever was monitored. After each successive increment, the fiber was released to attain a mechanical equilibrium. The fibers typically reached equilibrium in less than 5 minutes, as was indicated by the constancy of the vertical deflection. During the first stages of incremental elevation of the cantilever, the deflection stayed at zero level after equilibration. We associate this first "zero-force" stage with straightening of the fiber. This transition from a loose to a stretched state is shown schematically in Figure 5. When the fiber was straightened, further elevation of the cantilever resulted in deflection of the cantilever tip. The cantilever tip was used as an indicator of fiber deformation; by measuring the tip deflection and knowing the force constant of the cantilever, we estimated the fiber stiffness.

As follows from the schematic in Figure 5B-C, if L_0 is the fiber length before deformation, Δx is the vertical deflection of the cantilever tip, and ΔL is the fiber elongation, then the incremental change of the cantilever position after n steps is $\Delta x + \Delta L = n\delta$, where δ is the incremental elevation of the cantilever; $\delta = 1$ μm in our experiments. Cantilever deflection was calculated from the voltage reading corresponding to the vertical deflection. Deflection sensitivity was determined prior to the experiment. Using measured Δx, ΔL was obtained at each step n. The force was calculated as $F = k\Delta x$, where k is the force constant of the AFM cantilever (NSC11, MikroMasch Inc). With the given force, the Young's modulus was estimated as $E = F^*L_0/(\Delta L^*S)$, where S is the fiber cross-sectional area before deformation. It is expected that the cross-sectional area will decrease upon deformation; therefore these moduli provide a lower estimate of the materials elasticity.

The obtained results are presented in Figure 6A. The force–elongation curve has two parts with distinct slopes. This behavior is a typical mechanical signature of a porous material.[35] The first linear part of the curve corresponds to the initial fiber extension, when the pore walls buckle under a weak force. The corresponding modulus is very small, about $E \sim 1.5$ MPa, which is significantly lower than the elastic modulus of solid PVDF fibers and films, $E_f \sim 3.5$ GPa,[36] confirming that the fiber is highly porous. The second asymptotic region of deformation is associated with the material densification and pore collapse, which results in the material hardening. In this extension regime, the Young's modulus is almost two orders of magnitude greater, $E_f{}^h \sim 50$ MPa.

By weakening the elastic properties of single fibers, one weakens the elastic properties of the whole yarn. For a quantitative evaluation of the reduction of the yarn elastic modulus, we measured the bending modulus of the yarn. The yarn was horizontally suspended and clamped from one end, while the other end was loaded with different weight. Tip deflection *versus* applied weight was analyzed using the Euler elastica equations.[37] Assuming that all fibers in each yarn cross-section deform

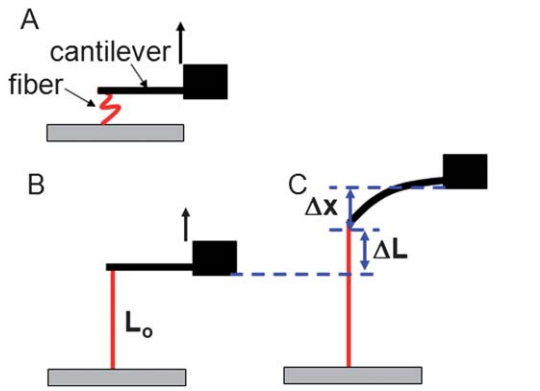

Fig. 5 Schematic of experimental protocol to study mechanical properties of single fibers with AFM.

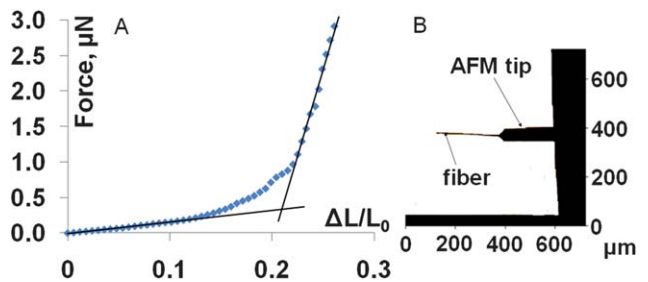

Fig. 6 (A) The force–elongation curve of the PVDF/PEO fiber (B) An optical image of a single PVDF/PEO nanofiber attached to the AFM tip.

uniformly, one would expect that each single fiber in the bent yarn is subject to small strains corresponding to the first linear part of the force–elongation curve. While the modulus of a single fiber was about $E \sim 1.5$ MPa, we found that the Young's modulus of the 80–150 μm diameter yarns varied between $E_y \sim 50$–220 MPa, depending on the compaction density of fibers in the yarn. This significant difference between elastic properties of a single fiber and those of yarns was also observed on textile yarns.[38] The effect was explained by the non-uniform distribution of tensile stresses in the yarn.[38,39] That is, after yarn twisting, the fibers that are situated closer to the yarn surface become more stretched than those sitting in the core. Therefore, one cannot assume that all fibers in the yarn cross-section are subject to the same strain: the fibers at the outermost layers of the yarn are most likely to be pre-deformed. When the yarn bends, these pre-deformed fibers follow the second asymptotic branch of the force–elongation curve with the greater modulus. The yarn as a coherent structure responds upon the bending stress with this increased modulus. Still, these yarns are much more flexible than solid textile fibers and yarns, which typically have Young's moduli measured in the gigapascal range.[39]

Absorption and transport properties of artificial proboscises

Fiber porosity. To determine the fiber porosity, a micropiece of as-spun fiber was cut using the tip of the AFM (Dimension 3100 AFM, Veeco Inc). Then, this piece was glued to the AFM tip for further analysis, Figure 6B. The idea of porosity measurements using AFM is that the resonance frequency of the AFM cantilever is very sensitive to minute changes in mass. If one manages to fill all pores in the attached fiber with certain liquid of a known density, the resonance frequency should depend on the mass of absorbed liquid, *i.e.* on its volume (see Methods). Hence the porosity, which is the ratio of the pore volume to the fiber volume, can be estimated directly. To confirm that the liquid is wicked into the pores and is not absorbed by the PVDF fiber itself, we conducted a series of experiments on films of the same composition. We confirmed that at time increments shorter than the time of droplet disappearance—which is ~20 minutes—the swelling of PVDF/PEO films is not significant, less than 5%. Therefore, one can safely neglect the swelling effect and interpret the experiments based on physical flow phenomena.

Assuming that all pores are filled completely with the liquid, the fiber porosity is estimated as

$$\varepsilon_f = \frac{V_{liquid}}{V_{liquid} + V_{matrix}} = \frac{1}{1 + V_{matrix}/V_{liquid}} = \frac{1}{1 + V_{matrix}\,\rho_{liquid}/M_{liquid}} \quad (1)$$

where V_{liquid} is the volume of absorbed liquid which is equal to the volume of pores and V_{matrix} is the volume of polymer matrix calculated through the fiber mass, mass fractions (M) of the used polymers, and their densities (ρ) as

$$V_{matrix} = V_{PEO} + V_{PVDF} = \frac{M_{PEO}}{M_{PEO} + M_{PVDF}} \frac{M_{fiber}}{\rho_{PEO}} + \frac{M_{PVDF}}{M_{PEO} + M_{PVDF}} \frac{M_{fiber}}{\rho_{PVDF}} \quad (2)$$

To ensure complete filling of nanopores in the fiber, we chose Galwick (Porous Materials, Inc) as the filler. Galwick has very low surface tension ($\sigma = 16$ dynes/cm^2) and it wets PVDF and PEO surfaces completely. Using AFM, the tip with attached fiber was immersed into a Galwick drop. Then, the new value of the resonance frequency was measured. Since the elastic constant of this complex spring is maintained, the change of the resonance frequency is mostly controlled by the added mass. We thus measured $M_{Galwick}$ and M_{fiber}. Substituting in equations (1) and (2) the measured ratio $M_{galwick}/M_{fiber} = 5.12$, and the given values $M_{PEO}/M_{PVDF} = 0.1$, $\rho_{Galwick} = 1.8212$ g/cm^3, $\rho_{PVDF} = 1.76$ g/cm^3, $\rho_{PEO} = 1.13$ g/cm^3, we estimated the porosity of single fibers as $\varepsilon_f = 0.82$. This high porosity suggests that even a single fiber appears to be a good candidate for design of nanoprobes enabling one to collect and retain liquids in pores. When the fibers are twisted in the yarn, thus forming large micropores between them, one expects that the transport properties of yarns will be significantly enhanced.

Absorbency of artificial proboscises

When the dimensions of pores in a material are measured in nanometers, the rate of wicking becomes very slow.[10–12,40–41]

Therefore, it is a challenge to speed up fluid transport in these materials. Integration of nanoporous fibers into yarns provides a new degree of freedom in the probe design. Yarns may have two types of pores: nanometer pores in the fibers and micrometer pores between the fibers. Therewith, the absorption kinetics is expected to be distinguishable from that observed in materials having a unimodal pore size distribution.[42]

In a first series of experiments we confirmed that the wicking properties of the produced yarns are reproducible. Droplets of wetting nonvolatile liquids, hexadecane (HEX) and tributyl phosphate (TBP), Table 1, were used for the evaluation of wicking properties of the yarns. These liquids were chosen as simulants of hazardous liquids. Droplets with initial volume V_0 were deposited on yarns, as shown in Figure 7A. The drop volume $V(t)$ was defined at each increment of time t by fitting the drop profile with Carrol's unduloid,[43,44] an analytical solution of the Laplace equation of capillarity that describes the drop shape as a function of its volume. Figure 7A shows a sequence of pictures of a hexadecane droplet during its absorption by the yarn. To confirm that the droplet does not evaporate during absorption experiments, but gets absorbed by the yarn, a reference hexadecane droplet was placed on a copper wire. As clearly seen from Figure 7A, this reference droplet does not change its volume appreciably, thus, proving that the yarn does take the drop in. The change of the droplet volume (V_0-$V(t)$) as a function of time was filmed and analyzed. Figure 7B shows the results of these absorption experiments conducted on four porous yarns. The absorption kinetics for both tested liquids followed the square-root-of-time law, also known as the Lucas–Washburn law.[45,46] The slope fitting lines in Figure 7B or wicking constants, are close to each other, further suggesting that the yarn properties are very repeatable from one sample to another and that the given similarity is not just a chance event, but an expected consequence of the similarity of liquid properties, Table 1.

In a second series of experiments, with three porous and three non-porous yarns, we showed that the absorption properties of yarns made of solid non-porous fibers are very much

Table 1 Properties of probed liquids

Property at (20°C-25°C)	Tributyl phosphate (TBP)	n-Hexadecane (HEX)
Color	Colorless	Colorless
Molecular formula (Molecular Weight)	$C_{12}H_{27}O_4P$ (Mw: 266.31)	$C_{16}H_{34}$ (Mw: 226.238)
Viscosity (mPa·s)	3.80	3.03
Surface tension (mN/m)	31.7 (measured: 29.94)	27.47 (measured: 23.28)
Density (g/cm^3)	0.97	0.773
Vapor Pressure (mm Hg)	2.6×10^{-6} @ 25 °C; 27 @ 178 °C	1 @ 105 °C

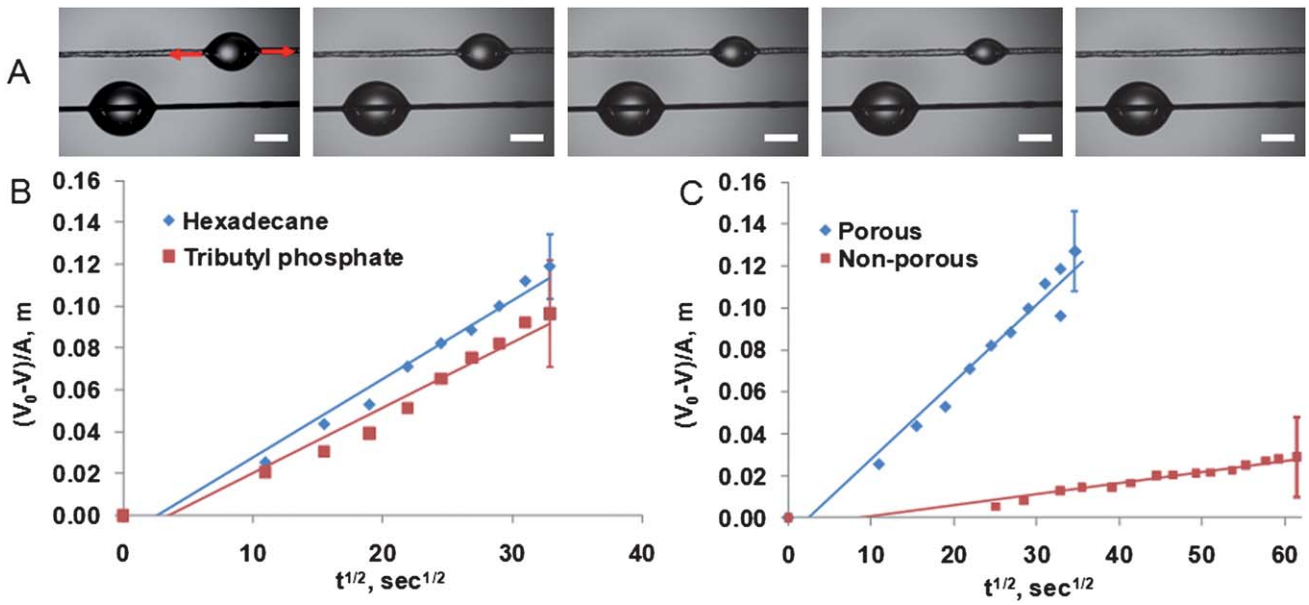

Fig. 7 (A) A series of pictures illustrating the wicking kinetics of a hexadecane droplet (~4 microliters) into the PVDF/PEO yarn (upper) made of nanoporous fibers. An 80 μm copper wire (lower) with a hexadecane droplet was used as the reference. The arrows show that the drop penetrates into the yarn in both directions. The scale bar is 500 μm (B) Comparative absorption kinetics of hexadecane and TBP droplets by yarns made of porous PVDF/PEO fibers. A is the yarn cross-section, V_0 is the initial drop volume, and V is the drop volume at time t. (C) Comparative absorption kinetics of hexadecane droplets by yarns made of porous and non-porous fibers. The error bar corresponds to the highest standard deviation in the experiments.

different from those of porous fibers. As demonstrated in Figure 7C, the wicking constant of yarns made of solid nonporous fibers is significantly smaller. It is, therefore, important to understand the mechanism of significant enhancement of the wicking properties provided by the nanoporous fibers in the yarn.

Mechanism of strong wicking

Nanoporous materials are superior absorbers due to their ability to generate extremely high capillary pressure.[47] The suction capillary pressure of a porous material is estimated by the Laplace formula as $P_c \sim 2\sigma\cos\theta/r_p$, where σ is the surface tension, θ is the contact angle, and r_p is a characteristic radius of pores in the material.[47,48] Hence, by decreasing the pore radius down to nanometers, one can significantly increase the driving force for the liquid wicking. On the other hand, doing so, one makes nanoporous materials even less permeable. Therefore, it is instructive to analyze a condition in which the interfiber spacing would provide sufficient permeability to the yarn, yet nanoporous fibers would increase the driving force for wicking. In other words, one needs to modify the Lucas–Washburn law to take into account the double porosity of the material.[42]

Typically, flow through nano and micrometer pores follows Darcy's law,[11,48] which assumes that the flow velocity is proportional to the pressure gradient, $q = -(k/\eta\nabla P)$, where k is the material permeability, η is fluid viscosity and P is the pressure. Following the Lucas–Washburn arguments, but introducing two porosities, ε_f and ε_y, and two permeabilities, k_f and k_y, the change of the droplet volume V with time t is described as $(V_0 - V)/A = c\sqrt{t}$, where c is the wicking constant derived in Methods,

$$c = 2\sqrt{2k_{eff}P_c/\eta}, \qquad k_{eff} = \left[k_y + (1-\varepsilon_y)k_f\right]\left[\varepsilon_y + (1-\varepsilon_y)\varepsilon_f\right] \tag{3}$$

The index f corresponds to the pores inside fibers, and y corresponds to the pores between fibers. The yarn porosity ε_y and permeability k_y, are considered the porosity and permeability of the yarn made of solid non-porous fibers. Equation (3) is a familiar definition of the Lucas–Washburn wicking constant

with the effective permeability k_{eff}. Capillary pressure P_c and effective permeability k_{eff} include all effects caused by nanopores in the fibers. As known from the physics of flow through porous media, the permeability is proportional to the square of the pore radius.[48] Therefore, the yarn permeability is typically much greater than the fiber permeability, $k_y \gg k_f$. In this limit, the wicking constant is represented in a form convenient for comparison with the experiment:

$$c = 2\sqrt{\frac{2P_c k_y}{\eta}\left[\varepsilon_y + (1-\varepsilon_y)\varepsilon_f\right]} \quad (4)$$

Porous fibers increase the capillary pressure, $P_c \propto 1/r_p$ but decrease the permeability, $k_f \propto r_p^2$. As follows from Equation (4), when the porous fibers are twisted in a yarn, the permeability increases, yet the capillary pressure stays the same. As a result, the wicking constant increases; the smaller the pore size in each fiber, the greater is the wicking constant.

As seen from Figure 4C, where the porosity of a spot not affected by the yarn cutting was analyzed, the fibers in the yarn are closely packed. It is therefore plausible to assume that the fibers form a hexagonal elementary cell. Then the yarn porosity is estimated as $\varepsilon_y \approx (\sqrt{3} - \pi/2)/\sqrt{3} \approx 0.1$, and its permeability as $k_y \approx 0.008\, d^2$, where d is the fiber diameter.[40] Keeping the ratio d/r_p high, one can significantly increase the wicking constant $\propto d/\sqrt{r_p}$. These arguments explain the experimentally observed tendency.

To make a quantitative estimate of the characteristic pore diameter, $D_p = 2r_p$, that pulls the liquid in the yarn, we solve Equation (4) for P_c and use the measured wicking constants c and fiber porosities, $\varepsilon_f \approx 0.8$. Through these parameters, the capillary pressure is expressed as $P_c = c^2\eta/[8k_y(\varepsilon_y + (1 - \varepsilon_y)\varepsilon_f]$. TBP and hexadecane wet the fibers, hence we can approximate the cosine of the contact angle by one, $\cos\theta \approx 1$. Therefore, the effective diameter of the pores in the fiber are estimated as

$$D_p \approx 4\sigma/P_c = 32\sigma k_y(\varepsilon_y + (1 - \varepsilon_y)\varepsilon_f)/(c^2\eta) \quad (5)$$

In experiments, the fiber diameters in the yarn varied from 0.7 to 1.5 μm with the average $d \sim 1$ μm. For the yarns made of solid fibers, $\varepsilon_f = 0$, with the average fiber diameter $d = 1$ μm, Equation (5) gives the diameter of effective pores as $D_p = 800$ nm. For yarns made of porous fibers, $\varepsilon_f \approx 0.8$, with the average fiber diameter $d = 1$ μm, Equation (5) gives the diameter of effective pores as $D_p = 100$ nm. The smaller diameter fits the size of the pores in each fiber and the larger diameter appears to be on the same order of magnitude as that of an average interfiber gap.

To confirm these estimates, we used the ImageJ (NIH) subroutine to evaluate the pore size distribution from the SEM pictures (Figure 4B) of porous fibers. Modeling the pore as a circular cylinder allowed calculating the pore diameter as $D_p = \sqrt{4A/\pi}$, where A is the visible cross-sectional area of the pore. Figure 8 shows that the average pore diameter is $D_p \sim 98$ nm, which is in agreement with the prediction of our theoretical model (~100 nm).

Thus, in our experiments, the hundred-nanometer pores provided the driving force for liquid wicking whereas micrometer-wide interfiber gaps facilitated the liquid movement through the yarns.

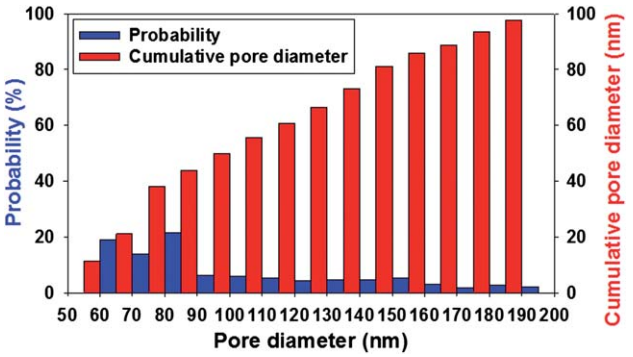

Fig. 8 The pore size distribution of electrospun nanoporous PVDF/PEO fibers. The blue column shows the frequency of appearance of a fiber with a certain diameter.

Deployment and manipulation with the artificial proboscis by applying electric field

A butterfly uses a yet unknown mechanism to unroll and direct its proboscis toward a target.[49] For the deployment and positioning of the artificial proboscis made of PVDF/PEO porous fibers, we take advantage of the PVDF ferroelectricity that is generated as a result of the electrospinning process. Hence the artificial proboscis can be flexed and controlled by applying an electric field. As shown in Figure 9, two copper plates were placed and fixed vertically and parallel to each other, forming an 18-mm gap in between. One plate was connected to a power supply (Glassman FC series) and the other plate was grounded. The 320 μm diameter artificial proboscis was vertically suspended between the two electrodes. Its upper end was clamped to the holder and the lower end was free to move. A 0.34 μL TBP droplet was deposited onto the substrate at the bottom of the cell. This cell was enclosed with a transparent 60 × 30 × 18 mm box, thus preventing any perturbations of the artificial proboscis caused by air flow. After application of an 8 kV potential, we observed proboscis flexion and the movement of its free end toward the droplet. In this field, no appreciable change of the droplet shape was observed. This process was filmed with a video camera (Dalsa Falcon 1.4, Canada). When the artificial proboscis touched the droplet, we turned off the power. After that, the tip of the artificial proboscis was held attached to the droplet by only the surface tension of the liquid. Finally, when the droplet was completely wicked into the yarn, the yarn bent back to its initial straight shape. Remarkably, the nylon yarn suspended in the cell as a reference stayed straight during the whole experiment (Figure 9). The nylon reference yarn had the same diameter and length as its experimental counterpart. This evidence favors the hypothesis that the PVDF/PEO fibers do contain a substantial amount of ferroelectric crystals. The question of reversibility of the process of yarn bending-strengthening deserves a special attention.

Thus, an artificial proboscis so constructed can be used for grabbing and probing hazardous liquids. Furthermore, it appears straightforward to embed superparamagnetic nanoparticles

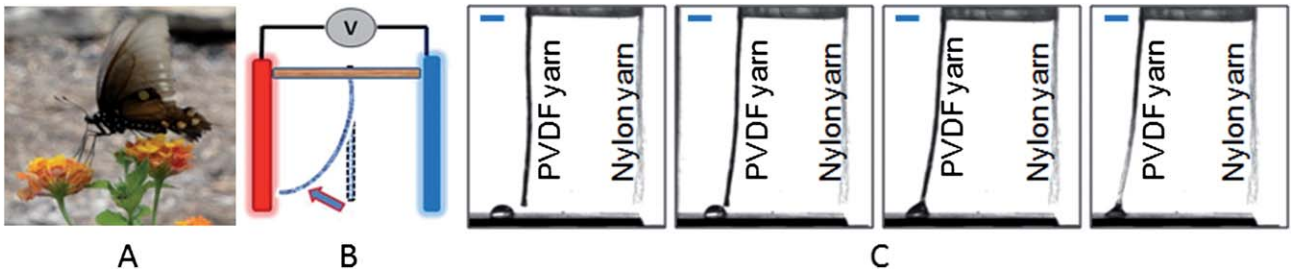

Fig. 9 (A) Butterfly with a proboscis searching for food. (B) A schematic of yarn manipulation with electric field generated by two vertical electrodes. (C) Artificial proboscis absorbing a TBP droplet. Two electrodes are positioned from the sides and are not shown here. The solid black fiber on the left is the artificial proboscis; the gray fiber on the right is a nylon yarn. The scale bar is 2 mm.

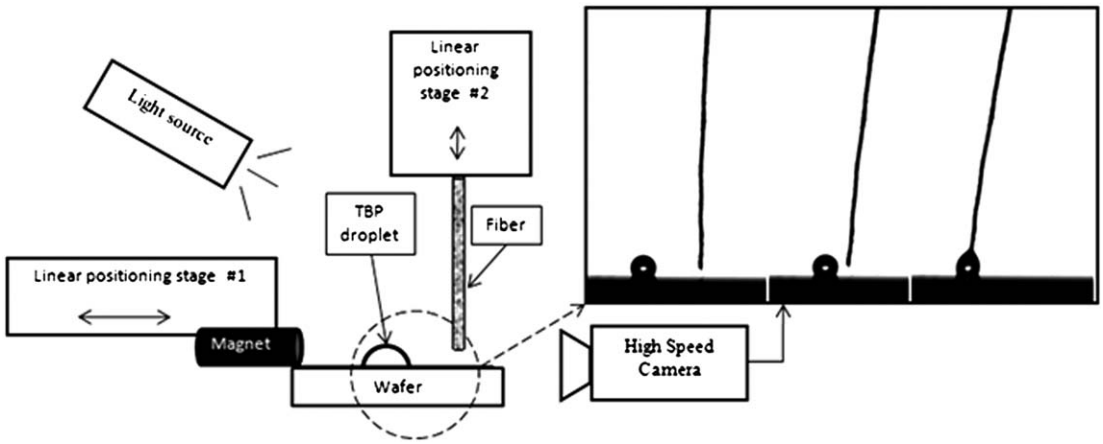

Fig. 10 Absorption of a TBP droplet by the artificial proboscis with embedded superparamagnetic nanoparticles. The proboscis was manipulated with a magnetic field.

(CMS Magnetics) into porous fibers, thus making the proboscis reactive to a magnetic field.[50–52] An example of such a proboscis is shown in Figure 10. Magnetically actuated artificial proboscises are attractive candidates for probing aqueous solutions, blood or any biofluids that do not interfere with the magnetic field.

Methods

Probe manufacturing

Two g of PVDF (Goodfellow Corporation) and 0.2 g PEO (M_w = 1,000 kDa, Sigma–Aldrich) were dissolved in 10 g dimethylacetamide (DMAc) (Spectrum) at 55 °C. All chemicals were used as received without further purification. The prepared polymer solution was placed in a 10 mL syringe. A flexible syringe heater (Watlow, EHG SL10) was attached to the syringe to maintain the temperature at 55 °C. The syringe with its heater was placed on the syringe pump (New Era Pump System, NE-300). A rotating mandrel with four alumina bars separated from each other by 20 cm was used as a fiber collector. A high-voltage power supply (Glassman High Voltage, Inc.) was connected to the syringe through a stainless-steel needle (Gauge 20, EXEL) and a 35 cm wide gap separated the needle end from the nearest face of the mandrel. The flow rate was controlled at 0.2 mL/hr. A positive voltage varying between 8–10 kV was applied to the needle until a fiber jet and Taylor cone were produced. A second high-voltage power supply was attached to the collector and a negative charge of 1 kV was applied. The device for fiber collection consists of two $^3/_4$ inch diameter circular wire brushes, mounted co-axially and each attached to a miniature DC motor. The same device was used to form yarns by spinning the brushes in the opposite directions. The number of revolutions and the rate of twisting was controlled with totalizer counters (Crouzet 2108) and optical reflection sensors (OPTEC Technology OPB704WZ) operating in the infrared range of light, thus avoiding any interference with other devices. Solid non-porous fibers were obtained at 25–35% RH while porous fibers were obtained at 65% RH even without PEO removal. Fibers were prepared at ambient temperature, 23–25 °C.

Probe characterization by Fourier Transform Infrared Spectroscopy (FT-IR)

FT-IR spectra of the electrospun nanofiber yarns were measured on Nicolet 550 Magna-IR spectrometer in the 400–1000 cm^{-1} range of wave numbers. Figure 11A shows three different IR spectra of PVDF pellets, PVDF/PEO films obtained by dip coating of glass slides, and electrospun PVDF/PEO fibers. The $C_2H_2F_2$ molecular unit cells in the PVDF chain have net dipole moments, pointing from the electronegative fluorine to the hydrogen, and can crystallize forming different phases with different dipole orientations.[53] It is known that β-phase mostly consists of CF_2-CH_2 dipoles oriented in the same directions, *i.e.*, this phase is ferroelectric. In another phase, called α-phase, the dipoles are counter directed or form clusters with zero net

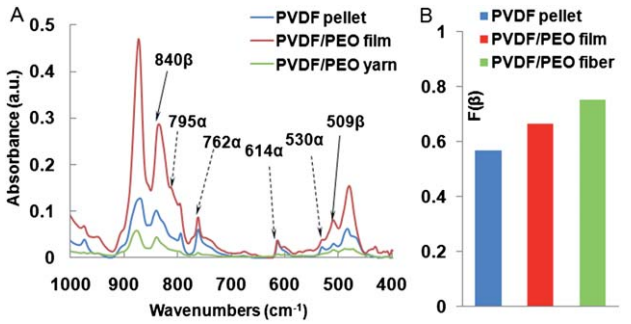

Fig. 11 (A) FTIR spectra of PVDF pellet, dip-coated PVDF/PEO film, and electrospun PVDF/PEO fiber. (B) β/α ratios for PVDF pellets, PVDF/PEO film and electrospun PVDF–PEO fibers, suggesting that the electrospun fibers contain greater amount of ferroelectric crystals.

moment, *i.e.*, this phase is not ferroelectric. β- and α-phases can be distinguished by their spectral characteristics: absorption bands of the β-phase are situated at 509 and 840 cm^{-1} and absorption bands of the α-phase appear at 530, 614, 762, and 795 cm^{-1}.[54–56] To estimate the fractional content of β- and α-phases in pellets, films and fibers, the fraction of β-phase in each sample was calculated using the Beer–Lambert law[54–56] in the form

$$A_\alpha = \log\frac{I_\alpha{}^0}{I_\alpha} = K_\alpha C X_\alpha L,\ A_\beta = \log\frac{I_\beta{}^0}{I_\beta} = K_\beta C X_\beta L, \quad (6)$$

where A_α and A_β are absorbencies of each phase, I^0 and I are the incident and transmitted radiation intensities, respectively, L is the sample thickness, C is the total monomer concentration, $K_{\alpha,\beta}$ are the absorption coefficients, and $X_{\alpha,\beta}$ are the mass fractions of the α- and β-crystals (sometimes called the degrees of crystallinity of each phase). In the literature, we were able to find only the absorption coefficients of PVDF measured at 762 and 840 cm^{-1} wavenumbers: $K_\alpha = 6.1 \times 10^4$ cm^2/mole and $K_\beta = 7.7 \times 10^4$ cm^2/mole.[54–56] Using these parameters, the relative fraction of the 840 cm^{-1} β- phase with respect to 762 cm^{-1} α- phases is given as

$$F(\beta) = \frac{X_\beta}{X_\alpha + X_\beta} = \frac{A_\beta}{(K_\beta/K_\alpha)A_\alpha + A_\beta} = \frac{A_\beta}{1.26A_\alpha + A_\beta} \quad (7)$$

The results are presented in Figure 11B. In the electrospun PVDF/PEO fibers, the fraction of β-crystals appears greater than that found in the PVDF pellets. Quantitatively, about 30% increase of the β-crystals was observed in electrospun fibers. This analysis suggests that electrospinning favors the formation of the β-phase in the nanofibers. This analysis, however, does not provide any information about the direction of the polarization vector in the fibers. One can assume that the polarization vectors in crystallites are randomly oriented, because the external field changed frequently owing to the mandrel rotation as well as because of flipping of the field directions between each pair of charged arms.

Fiber porosity

The quantitative estimate can be done using a simple spring model. If the AFM tip with attached fiber has mass M and the elastic constant of the cantilever spring is k, the tip oscillations in the vertical plane are described by the spring model as $M\,d^2y/dt^2 + ky = 0$, where y is the vertical coordinate of the tip center of mass, and t is the time, and oscillations are considered about the tip equilibrium position $y = 0$. Assuming sinusoidal oscillations of the form $y = a \sin(ft)$, where a is the tip amplitude, and f is its frequency, and substituting this form into the spring equation, we find the natural frequency as $f = \sqrt{k/M}$. When the cantilever is subjected to the forced oscillations, the oscillations become amplified as the frequency approaches the natural frequency f; hence this frequency is called the resonance frequency.[37] Therefore, one can measure the resonance frequency f of the cantilever with the dry fiber, and the resonance frequency $f_m = \sqrt{k/(M + M_{liquid})}$ of the cantilever with the fiber containing the liquid of mass M_{liquid}. The mass of liquid can be found as $M_{liquid} = (k/f_m^2)[1 - (f_m/f)^2]$. If the resonance frequency of the cantilever without fiber is f_{AFM}, the fiber mass M_{fiber} can be found as $M_{fiber} = (k/f^2)[1 - (f/f_{AFM})^2]$. Therefore, from these experiments, the mass of fiber and absorbed liquid can be obtained.

Kinetics of drop absorption into yarns with double porosity

If the yarn cross-sectional area is A, the velocity of the wetting front at time t is $U(t)$, then the flow discharge through the interfiber pores is calculated as $Q_y = \varepsilon_y A U(t)$. The cross-sectional area of the fibers in the yarn is obtained as $A_f = (1 - \varepsilon_y)A$. Accordingly, the flow discharge through the porous fibers reads $Q_f = \varepsilon_f A_f U(t) = (1 - \varepsilon_y)\varepsilon_f A U(t)$. Due to definition, the yarn permeability k_y corresponds to the permeability of yarn made of non-porous fibers, $Q_y = -(\partial P/\partial x)(k_y A/\eta)$. If the permeability of a single porous fiber is k_f, the discharge only through the fibers is obtained through Darcy's law as $Q_f = -(\partial P/\partial x)(k_f A_f/\eta)$. Thus, the mass balance reads

$$\left[\varepsilon_y + (1 - \varepsilon_y)\varepsilon_f\right] A U(t) = -\frac{1}{\eta}\frac{\partial P}{\partial x}\left(k_y + (1 - \varepsilon_y)k_f\right)A \quad (8)$$

Directing the x-axis along the fiber, we write the continuity equation for the flow inside the yarn as $\partial(Q_y + Q_f) = 0$. From Darcy's law, it directly follows that the pressure gradient is a function of time only, $\partial P/\partial x = G(t)$. To find this function $G(t)$, we need to specify the boundary conditions. Examining Figure 7A, we notice that the drop length does not change during adsorption. Since two contact lines bounding the drop separate the regions with positive (drop) and negative (yarn) pressures, the pressure is atmospheric at these contact lines.[10] For further analysis it is sufficient to consider only one half of the drop and place the center of coordinate at the contact line. Hence, taking atmospheric pressure for the reference, the first boundary condition reads $P(0) = 0$. The second boundary condition is formulated at the wetting front $x = L(t)$. There, the capillary pressure is built by the pores inside individual fibers, $P(L) = -P_c$. These two boundary conditions specify the pressure gradient, $G(t) = -P_c/L(t)$. Substituting this pressure gradient and noticing that at the wetting front $U(t) = dL/dt$, Equation (8) is reduced to an ordinary differential equation that can be integrated once to give

$$L^2 = \frac{2P_c}{\eta}\frac{(k_y + (1 - \varepsilon_y)k_f)}{[\varepsilon_y + (1 - \varepsilon_y)\varepsilon_f]}t \quad (9)$$

The front position L(t) can be expressed through the incremental change of droplet volume as: $(V(t) - V_0)/A = 2(\varepsilon_y + (1 - \varepsilon_y)\varepsilon_f)\,L(t)$,

where the factor two accounts for two wetting fronts. Solving this equation for $L(t)$ and substituting it to Equation (9), we obtain Equation (4).

Analysis of pore size distribution

The pore size distribution was analyzed by using ImageJ software (NIH). The images from Figure 4B were cropped into several 2 μm × 1 μm pieces and the number of pores in each picture was calculated. ImageJ also provides the pore area. To estimate the pore diameter, we assumed that all pores were made of circular cylinders with diameter d. Figure 8 shows that most pores had the diameters in the range of 60∼80 nm. The average diameter was calculated from $D_p = \Sigma f_i * d_i$, where f is the probability to find the diameter d_i, and subscript i corresponds to the site at which the pore diameter was measured within the prescribed range from 50 to 190 nm.

Conclusion

We developed a technique to fabricate artificial proboscises. PVDF/PEO fibers have been electrospun into ordered bands and subsequently twisted into yarns. By controlling the electrospinning time and revolution rate of the proposed twisting device, we formed biomimetic probes with repeatable transport and mechanical properties. By varying the chemical composition of polymer blends and environmental conditions for electrospinning, we achieved porosities as high as 82% for single fibers. As predicted theoretically, and proven experimentally, the absorption rate of the probes can be significantly increased if one designs the probes to have double porosity composed of micro- and nanopores. Depending on the application, the probe can be made ferroelectric or magnetic. Further, we showed that owing to the ferroelectric and magnetic properties of the probes produced in this work, these probes can function as artificial proboscises and can be manipulated remotely to absorb droplets. Commercially available microfluidic devices are typically monolithic stationary platforms with multiple channels to which the liquid is delivered either by a pipette or by a pump. We believe that the paradigm of a stationary microfluidic platform can be shifted to the flexible structures using the proposed strategy and materials. One should mention that the produced materials swell in hours after a TBP or hexadecane droplet gets inside. Since these liquids are simulants of many hazardous plasticizers, we expect that the field-induced bending of the PVDF yarns will be affected. Thus, these probes can be used as sensors as well. This work has the potential to embed multiple sensing devices in a single fiber and make the probing device in the form of an artificial octopus with many different microarms probing and analyzing the substrate in different places simultaneously. The fiber-based flexible platform here developed opens up many opportunities for probing and manipulating hazardous liquids, extracting biofluids from microorganisms or secretory glands, or operating on single cells.

Acknowledgements

We acknowledge the support from NSF grants CMMI-0826067 and CMMI-0825773, EFRI 0937985, and the U.S. Air Force contract FA8650-09-D-5900. D. Lukas and P. Mikes acknowledge the support from The Ministry of Interior of the Czech Republic, grant no. (BV II/2-VS) 1656.

Notes and references

1 D. Monaenkova, M. S. Lehnert, T. Andrukh, C. E. Beard, B. Rubin, A. Tokarev, W.-K. Lee, P. H. Adler and K. G. Kornev, Butterfly proboscis: combining a drinking straw with a nanosponge facilitated diversification of feeding habits, *J. R. Soc. Interface*, 2011, DOI: 10.1098/rsif.2011.0392.
2 D. H. Reneker, A. L. Yarin, E. Zussman and H. Xu, *Adv. Appl. Mech.*, 2007, **41**, 43–195.
3 D. H. Reneker and A. L. Yarin, *Polymer*, 2008, **49**, 2387–2425.
4 Y. Dzenis, *Science*, 2008, **319**, 419–420.
5 G. C. Rutledge and S. V. Fridrikh, *Adv. Drug Delivery Rev.*, 2007, **59**, 1384–1391.
6 J. Fang, H. T. Niu, T. Lin and X. G. Wang, *Chin. Sci. Bull.*, 2008, **53**, 2265–2286.
7 E. M. Janle and J. E. Sojka, *Contemporary Top. Lab. Animal Sci.*, 2000, **39**, 47–50.
8 C. M. Huang, C. C. Wang, M. Kawai, S. Barnes and C. A. Elmets, *J. Chromatogr., A*, 2006, **1109**, 144–151.
9 V. Reukov, A. Vertegel, O. Burtovyy, K. G. Kornev and I. Luzinov, *Mater. Sci. Eng. C*, 2009, **29**, 669–673.
10 D. Monaenkova and K. G. Kornev, *J. Colloid Interface Sci.*, 2010, **348**, 240–249.
11 G. Callegari, I. Tyomkin, K. G. Kornev, A. V. Neimark and Y. L. Hsieh, *J. Colloid Interface Sci.*, 2011, **353**, 290–293.
12 K. G. Kornev, X. Ren and Y. Dzenis, *Journal of Engineered Fibers and Fabrics*, 2009, **4**, 14–23.
13 A. M. Afifi, S. Nakano, H. Yamane and Y. Kimura, *Macromol. Mater. Eng.*, 2010, **295**, 660–665.
14 K. Zhang, X. F. Wang, Y. Yang, L. L. Wang, M. F. Zhu, B. S. Hsiao and B. Chu, *J. Polym. Sci., Part B: Polym. Phys.*, 2010, **48**, 1118–1125.
15 F. Dabirian and S. A. H. Ravandi, *Fibres Text. Eastern Eur.*, 2009, **17**, 45–47.
16 M. B. Bazbouz and G. K. Stylios, *Eur. Polym. J.*, 2008, **44**, 1–12.
17 A. Mondal, R. Borah, A. Mukherjee, S. Basu, M. Jassal and A. K. Agrawal, *J. Appl. Polym. Sci.*, 2008, **110**, 603–607.
18 F. L. Zhou and R. H. Gong, *Polym. Int.*, 2008, **57**, 837–845.
19 S. Moon and R. J. Farris, *Polym. Eng. Sci.*, 2007, **47**, 1530–1535.
20 E. Smit, U. Buttner and R. D. Sanderson, *Polymer*, 2005, **46**, 2419–2423.
21 W. E. Teo and S. Ramakrishna, *Nanotechnology*, 2006, **17**, R89–R106.
22 K. Adu-Wusu and N. M. Hassan, *Sep. Sci. Technol.*, 2005, **40**, 463–482.
23 J. A. Carrera, E. Munoz, E. Bringas, M. F. San Roman and I. Ortiz, *Desalination*, 2009, **245**, 675–679.
24 R. A. Kumbasar, *J. Membr. Sci.*, 2009, **338**, 182–188.
25 R. A. Kumbasar, *J. Hazard. Mater*, 2010, **178**, 875–882.
26 N. Messikh, M. H. Samar and L. Messikh, *Desalination*, 2007, **208**, 42–48.
27 I. Ortiz, E. Bringas, M. F. San Roman and A. M. Urtiaga, *Sep. Sci. Technol.*, 2005, **39**, 2441–2455.
28 L. F. Zhao, D. J. Fei, Y. G. Dang, X. L. Zhou and J. L. Xiao, *J. Hazard. Mater.*, 2010, **178**, 130–135.
29 Y. Filatov, A. Budyka and V. Kirichenko, *Electrospinning of micro- and nanofibers: fundamentals in separation and filtration processes*, Begell House Inc, New York, 2007.
30 H. T. Niu, T. Lin and X. G. Wang, *J. Appl. Polym. Sci.*, 2009, **114**, 3524–3530.
31 X. Wang, H. T. Niu, T. Lin and X. G. Wang, *Polym. Eng. Sci.*, 2009, **49**, 1582–1586.
32 D. Li, Y. L. Wang and Y. N. Xia, *Nano Lett.*, 2003, **3**, 1167–1171.
33 E. Zussman, M. Burman, A. L. Yarin, R. Khalfin and Y. Cohen, *J. Polym. Sci., Part B: Polym. Phys.*, 2006, **44**, 1482–1489.
34 R. Burtovyy, Y. Liu, B. Zdyrko, A. Tregub, M. Moinpour, M. Buehler and I. Luzinov, *J. Electrochem. Soc.*, 2007, **154**, H476–H485.
35 L. J. Gibson and M. F. Ashby, *Cellular Solids: Structure and Properties*, Cambridge University Press, New York, 1999.
36 C. Du, B. Zhu and Y. Xu, *J. Mater. Sci.*, 2005, **40**, 1035–1036.

37 L. D. Landau and E. M. Lifshitz, *Theory of elasticity*, Pergamon, New York, 1970.
38 J. W. S. Hearle, in *Structural mechanics of fibers, yarns, and fabrics*, eds. J. W. S. Hearle, P. Grosberg and S. Backer, Wiley, New York, 1969, **vol. 1**, pp. 213–255.
39 T. Hongu, G. O. Phillips and M. Takigami, *New millenium fibers, Woodhead Publishing Ltd*, Cambridge, England, 2005.
40 A. V. Neimark, S. Ruetsch, K. G. Kornev, P. I. Ravikovitch, P. Poulin, S. Badaire and M. Maugey, *Nano Lett.*, 2003, **3**, 419–423.
41 N. R. Raravikar, L. S. Schadler, A. Vijayaraghavan, Y. P. Zhao, B. Q. Wei and P. M. Ajayan, *Chem. Mater.*, 2005, **17**, 974–983.
42 M. M. Alimov and K. G. Kornev, *Phys. Fluids*, 2007, **19**, 102108.
43 B. J. Carroll, *J. Colloid Interface Sci.*, 1976, **57**, 488–495.
44 X. M. Chen, K. G. Kornev, Y. K. Kamath and A. V. Neimark, *Text. Res. J.*, 2001, **71**, 862–869.
45 R. Lucas, *Kolloid-Z.*, 1918, **23**, 15–22.
46 E. W. Washburn, *Phys. Rev.*, 1921, **17**, 273–283.
47 F. Rouquerol, J. Rouquerol and K. Sing, *Adsorption by powders and porous solids*, Academic Press, New York, 1999.
48 A. E. Scheidegger, *The physics of flow through porous media*, University of Toronto, Toronto, 1974.
49 L. E. S. Eastham and Y. E. E. Eassa, *Philos. Trans. R. Soc. London, Ser. B*, 1955, **239**, 1–43.
50 G. Korneva, H. H. Ye, Y. Gogotsi, D. Halverson, G. Friedman, J. C. Bradley and K. G. Kornev, *Nano Lett.*, 2005, **5**, 879–884.
51 K. G. Kornev, D. Halverson, G. Korneva, Y. Gogotsi and G. Fridman, *Appl. Phys. Lett.*, 2008, **92**, 233117.
52 J. R. Freedman, D. Mattia, G. Korneva, Y. Gogotsi, G. Friedman and A. K. Fontecchio, *Appl. Phys. Lett.*, 2007, **90**, 103108.
53 M. Poulsen and S. Ducharme, *IEEE Trans. Dielectr. Electr. Insul.*, 2010, **17**, 1028–1035.
54 J. S. Andrew and D. R. Clarke, *Langmuir*, 2008, **24**, 670–672.
55 R. Gregorio and M. Cestari, *J. Polym. Sci., Part B: Polym. Phys.*, 1994, **32**, 859–870.
56 Y. Bormashenko, R. Pogreb, O. Stanevsky and E. Bormashenko, *Polym. Test.*, 2004, **23**, 791–796.